FACTA UNIVERSITATIS
Series: **Mechanical Engineering**
https://doi.org/10.22190/FUME221217008F

Original scientific paper

INVESTIGATION OF HEAT-AFFECTED ZONES OF THERMITE RAIL WELDINGS

Szabolcs Fischer[1], Dóra Harangozó[2], Dalma Németh[1], Bence Kocsis[2], Mykola Sysyn[3], Dmytro Kurhan[4], András Brautigam[5]

[1]Széchenyi István University,
Department of Transport Infrastructure and Water Resources Engineering, Hungary
[2]Széchenyi István University, Department of Materials Science and Technology, Hungary
[3]Technical University Dresden,
Department of Planning and Design of Railway Infrastructure, Germany
[4]Ukrainian State University of Science and Technologies,
Department of Transport Infrastructure, Ukraine
[5]Budapest Transport Privately Held Corporation (BKV), Hungary

Abstract. *The paper investigates the heat-affected zone (HAZ) of several rail joints executed by thermite rail welding (TW). The examined rail profile was 54E1 (UIC54). The rail steel categories were different: R260 and R400HT. The welding portions of the TWs fitted R350HT and R260 rail categories with normal welding gaps. The rail pieces were brand new, i.e., without any usage in the railway track. The authors executed Vickers-hardness tests (HV10) and material texture tests on the running surface of the rail head, as well as on slices cut from the rail head. The cutting was performed by the water jet method, five longitudinal direction slices with vertical cutting lines. The considered specimen lengths were 2×70 mm (i.e., 70 mm from the mid-point of the rail joint), however, the depths were 20 mm from the running surface. Therefore, the measuring spaces were 5 mm lengthwise and 2 mm in depth. The variation of the hardness values was determined considering the microstructures of the base steel material and the TW. For comparison, previously measured Elektrothermit SoW-5 and earlier own research were taken into consideration.*

Key words: *Thermite rail welding, Heat-affected zone, HAZ, Vickers hardness, Brinell hardness, Microstructure*

Received: December 17, 2022 / Accepted February 09, 2023
Corresponding author: Dóra Harangozó
Széchenyi István University, Audi Hungaria Faculty of Automotive Engineering, Department of Materials Science and Technology, H-9026 Győr, Egyetem tér 1., Hungary
E-mail: harangozo.dora@sze.hu

1. INTRODUCTION

Long-distance rail transport became one of the most important means of land transport in the 20th and 21st centuries. It is convenient, safe, fast, and generally has high punctuality, which of course, can vary considerably depending on the country and the railway company. Long-distance rail travel is generally worthwhile for distances above 500-1000 km, taking into account travel time, and is less competitive than air travel above this distance [1]. Of course, when travel costs are considered (in particular ticket and/or season ticket prices), it is at a significant disadvantage compared to so-called low-cost airlines. On the other hand, it is also worth considering that railway stations and passenger stations in large cities may be located in the center of the city, in the central core (even in the historic city center), thanks to the railway construction of the 18th and 19th centuries. In contrast, airports are usually located far from the cities. It can mean distances of up to 10-50 km. These relatively long distances can only be covered by additional public or private transport, which is a disadvantage for tourists and tourism.

In the years 2021-2023, the significant increase in electricity prices and fuel prices (e.g., diesel, kerosene, etc.) will create serious problems and difficulties for both countries and public and private (large) public transport companies (of course, the same can be said for private transport, where petrol, diesel, electricity, natural gas, etc. are the most relevant). The reasons, of course, are many: part of the explanations and justifications is seen in the current problematic political situation worldwide, another part in the prolonged COVID pandemic, and in the cyclical world economic stock market boom and bust, etc. However, the most plausible explanation may be a combination of the preceding, to a greater or lesser extent, i.e., no one factor can be neglected entirely.

Because of the above, it should be noted that transportation itself [2,3], among other things, the rail transport and railway lines are both critical and mandatory areas of major importance for the national economy.

In this article, the authors focus on one of the most critical elements of railway tracks: the rail track. In the following paragraphs, the authors have prepared a relevant literature review on railway tracks to present and summarize the essential literature findings on the subject.

Railway tracks consist of superstructure and substructure, but of course, other related structural elements can also be mentioned (e.g., catenary support columns, safety equipment elements, and components, etc.). If the discussion is restricted to railway tracks, the superstructure consists of the track and the ballast, and special elements of the track, e.g., siding, in the case of ballastless tracks. The substructure includes the additional layer, usually granular material, and the earthwork itself, usually soil material. The tracks' parts are the rails, rail fasteners, and sleepers. The vehicle load must be considered as dynamic, however, in some approximated calculations, only the static values can be considered [4].

It is proved that the higher the geometrical faults in the railway track, the more critical and higher the dynamic evolved effect due to them [4-10]. Of course, the vibration and the noise will increase, however, they are not only related to the geometrical faults [11] but the structure of the railway track [8-10], the rail dampers can be noted as one of the most relevant parts [12-13]. Of course, safety, as well as risk and economic analysis of railway projects, is an integral part of railway lines' design, construction, and operation [14].

This study focuses on rail connections (or, in other words, rail joints). The rails can be connected with the help of fishplates and bolts, as well as rail welding.

Modern rail production technologies and delivery options limit the length of rails up to a maximum of 120 meters (e.g., see the technology of Voest Alpine [15]). Therefore, rail joints are essential parts of railway systems to secure the continuity of the rails without vertical or horizontal drops or changing directions. Rail joints must bear dynamic loads and secure movements caused by dilatation without structural damage. In order to be feasible easily and fast, the joints should contain the less and most simple parts, which are also easy to maintain. Generally, rail joints are probably the weakest parts of rail tracks. Their malfunctions lead to dangerous situations and a high risk of accidents. Global and corporational (i.e., industrial) railway safety requirements control the applicability of the different types [16].

The original method of joining rails is using bolted rail joints (or, in other words: fishplated rail joints). It is a simple, fast, and cost-effective technology with the disadvantage of resulting in a high rate of failures since the bolts cause dynamic shocks in rail wheels, reducing their lifetime and producing noises [17]. To eliminate the high demand for the maintenance of bolted joints, engineers introduced welding techniques as new methods of rail joints in the early 1900s [18]. Against bolted joints, the dynamic behavior of the vehicle and the track is more beneficial and less expensive to maintain. Flash-butt welding (FBW) and alumino-thermic (thermite, TW) welding are the most commonly used welding technologies. FBW is based on electric resistance. The rail ends are heated by electricity (low voltage, approx. 15-25 V, and extremely high amperage, approx. 100,000-150,000 A) and hydraulically forged in a stationary plant. Then the sections of approx. 400 m can be transported to their final location [19]. However, another solution must be mentioned: the so-called welding machines on trucks or locomotives, which can weld the rails by FBW at the construction site. Therefore, the transportation of some hundred-meter-long rails can be avoided [16].

The TW technology is the most common method of joining and repairing rails on-site [20]. The technology was invented by a German professor of chemistry, Hans Goldschmidt, in 1895. He studied the reaction of metal oxides and aluminum for decades. The rail ends are melted by the heat (approx. 2200-2400 °C) emerging from the reaction of aluminum and iron-oxide [21,22]. Generally, the thermite welding material consists of 18-20% FeO and 79-85% Fe_2O_3 with an average grain size of 0.1-5 mm. Additional elements such as carbon, manganese, chromium, nickel, vanadium, and TiC may also be added to the mixture to produce similar characteristics to the rail to be welded. It is a fusion welding process since the melted iron flows into the gaps in the mold where the rail ends are welded together. During the exotherm reaction, metal oxides and aluminum become iron and aluminum oxide. By strictly controlling the parameters of the process (such as equipment, composition of the thermite material, preparation, and pre-heating of the rails), a weld free of macroscopic defects can be achieved with mechanical properties comparable to the "parent rail". This way, TW is an effective methodology of on-site joining rails without using electric power [16,23-24].

However, the microstructure of the rails and, thus, the mechanical properties are inevitably affected by the enormous heat arising during the welding process [23,25,26]. It is the so-called heat-affected zone (HAZ). Close to the centerline of the welding, the material reaches the recrystallization temperature. The austenitization of steel depends on the temperature and time of heating [27]. Therefore, zones close to the centerline are completely recrystallized, while only partial austenitization could happen at a certain

distance. Porcaro et al. [25] studied the microstructure of FBW. They discussed HAZ, which consists of three zones:

i. Close to the central line of the welding, a coarser grain size ferritic-pearlitic microstructure can be observed, which is a sign of decarburization.
ii. Grain growth region: the temperature was high enough to allow grain growth of austenite crystals.
iii. Grain refined region: completely recrystallized zone, but the temperature was not so high to coarsen the grain size.

Regarding the microstructural map of the welding, these zones are followed by the partially austenitized zone and the base metal.

Similarly to FBW, in the case of TW, the pearlitic main structure of the parent rail with a grain size of 5-6 may transform into a ferritic-pearlitic microstructure [28]. Retained austenite may also appear. Zones with coarser or finer grain sizes than the original may appear at different distances from the center line of the weld. The cementite of pearlite becomes spherical in the HAZ, reducing the rail's hardness and strength [29]. A zone with a higher hardness also exists in the HAZ, which can give rise to fatigue fracture [17,21,22]. In accordance with the microstructural changes, the hardness of the rail also alters. In general, a smaller grain size indicates higher hardness and thus reduces the joint's stiffness, which can lead to fatigue failures. Corser grain structure causes lower hardness and wear resistance, resulting in increased impact loading and premature welding failure [30]. Detailed studies of the hardness profile of FBW are published in [25,26]. 2 mm below the running surface, the hardness of the centerline of the welding is approx. 300 HV, which is decreased by 50 HV at a distance of 20 mm. The rolling technology of rails indicates a higher hardness on the rail web than on the head and the foot [26].

Compared to FBW, the coarse casted structure of TW joints means lower hardness making them less resistant to wear, but it can be improved by heat treatment [16]. The most spectacular advantage of heat treatment of TW joints is the improvement of tensile properties and the change of the fracture mechanism from brittle to ductile.

Examination of the vehicle-track contact dynamics and failure modes of rails is a topic of contemporary research [31,32]. Financial operations with efficient energy use are also popular research topics [33-35] regarding the problems of the 21st century. The most modern digital image correlation (DIC) measurement systems' applicability in mechanical engineering, materials science, and electronics has already been proven [36-40]. Recent research applies DIC to investigate a civil engineering problem [41]. As mentioned earlier, the rail joints are the weak points of rail tracks as they can be potential initiation points of failure. Besides traditional microstructure studies, current research focuses on the fracture mechanism of welded joints. [18-20,30,40-43] published detailed numerical studies and performed finite element analysis on the fatigue behavior of TW joints. These methods can be well adapted to predict the fatigue crack initiation, thus, the life cycle of rail welding.

Nowadays, newly developed types of rails are installed in rail tracks, claiming the need to join different rails without transitional parts. Welding of two rail ends with very different hardness may also be required. Test welds with transition rails have been prepared and analyzed in a material testing laboratory to examine the possibility of eliminating too low or too high hardness layers.

2. MATERIALS AND METHODS

During the research, laboratory hardness tests were executed on aluminothermic rail weldings prepared under non-laboratory conditions but with precise and accurate adherence to the technology.

For the tests, rails of different base hardnesses (R260 and R400HT, [46]) have been welded together. The rail profiles for both rail sections and weldings were 54E1 [46]. Two weldings have been prepared:

i. Sample #1: R260-R400HT with a normal non-heat treated welding portion for R260 rails and
ii. Sample #2: R260-R400HT with a heat-treated welding portion for R350HT rails (see (Fig 2.1.1).

Both weldings have normal welding gaps, i.e., 27-30 mm. In both cases, the rails were unloaded, i.e., brand new.

2.1 Preparatory work

In the preparation phase of non-track welding, the rail ends should be cleaned of dirt, and the welding gap set according to the technology (in terms of height and width, i.e., vertically and horizontally, respectively) (see Fig. 1).

Fig. 1 Setting the rail ends as a function of the welding gap

2.2 Preparation of the weldings

The execution of the rail welding procedure starts with preparing and unpacking the so-called welding set. Then the sand tray, the universal clamping device, and the molding elements (with mold clamping plates) are placed on the previously cleaned and adjusted rail ends. In all cases, the gaps must be sealed with sealing sand. After the slag tray has been installed, the rail head protection plate is also installed. The prepared pots are then placed on top, and the thermite can be loaded into them. In the case of low external temperatures, the rail ends must be pre-heated: usually, over 1-1 m from the rail ends. In

this study, this pre-heating was only applied for the rail ends, and the temperature was approx. 900 °C. Depending on external conditions and rail qualities, it may be necessary to partially preheat the rails over a longer section [47]. The procedure is as follows: fitting the burner head, ignition, pre-heating itself and then fitting the sealing element. Pre-heating is achieved with a propane-oxygen gas mixture (the pressure can vary between 1.50 and 4.0 bars. 1.50 bar is related to propane, and 4.0 bar is to oxygen).

After inserting the igniter into the thermite, the pot must be covered to allow the chemical reaction. Next, the thermite steel (the approx. temperature is 2000 °C) flows into a mold while the liquid slag flows into the tray.

When the slag solidifies, the tray and the pot can be removed. Finally, the mold clamping plates can be removed.

2.3 Post-production of the weldings

After the molds are unset, the excess material is removed with a press to half the height of the rail web, and after cooling, the residual material follows. The subsequent operation is rough grinding, followed by cleaning the welding. The final step is to carry out the finishing operation.

2.4 Sampling

The marking of the samples (based on Section 2) can be seen in Fig. 2. Slices have been taken under laboratory conditions from different parts of the rail head by water jet cutting (machine type: FLOW) in the laboratory. The samples were first cut into five equal slices (see Fig. 3) by waterjet. These slices were cut in half at the welding axis for further testing and then further cut into 7 cm long pieces (see Fig. 4) by a metallographic cutting machine. The sampling has not affected the measured results, as appropriate cooling of the metal has been ensured during the process.

Fig. 2 Marking of samples (in the front Sample #2, in the background Sample #1)

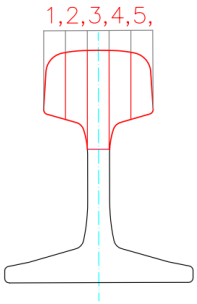

Fig. 3 The samples' rail heads are divided into five slices (the thickness is approximately 22 mm). The identifications will be in the following: from Slice #1 to Slice #5.

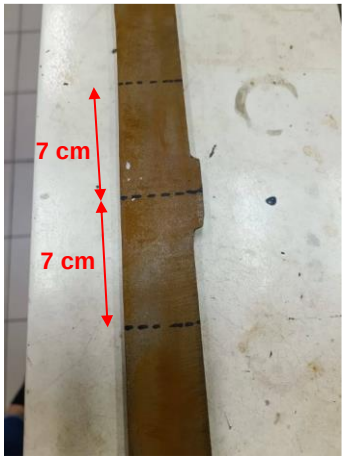

Fig. 4 The final specimen of 2×70 mm

Previous research [48,49] has demonstrated that critical points in the heat-affected zone can be found within 70 mm of the welding's axis (for normal-gap thermite welding, i.e., a welding gap of about 27-30 mm), and taking into account that the grinding and polishing equipment used to prepare the samples limited the length that could be tested in a single pass. It was for this reason that samples of 2×70 mm were created.

2.5 Metallographic preparation process

To be able to perform the hardness measurement and the microstructural analysis, the slices from the water jet cutting must be metal-cleaned so that machining grooves do not affect the accuracy of the measurements. For this reason, the surface must be "mirror-finished" for low-load tests.

Conventional steps of the metallographic preparation process:

1. wet grinding with silicon carbide sandpaper in multiple grades: P80, P180, P500, and finally, P800,

2. polishing of slices in multiple steps with diamond suspension: 9, 6, 3, and finally, 1 µm,
3. etching with nital (3% nitric acid, 97% ethyl alcohol) to reveal the microstructure.

The result of this preparation process is presented in Fig. 5. The structure of the weld and the HAZ are separated well in the macroscopic image.

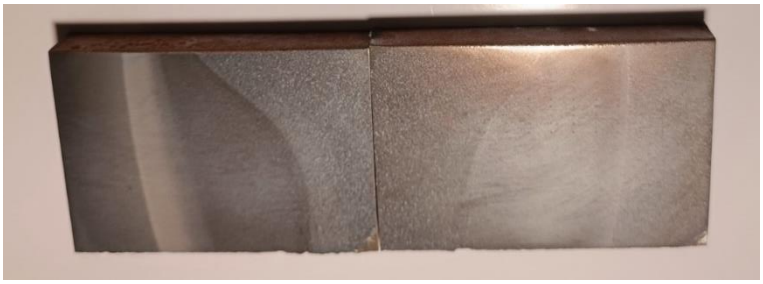

Fig. 5 The outlined microstructure (Sample #1, Slice #3)

2.6 Hardness tests

Vickers hardness values have been determined by applying F=98.07 N force according to the specifications of MSZ EN ISO 6507-1:2018 [50]. These values have been converted to HB (i.e., Brinell hardness). Furthermore, HB hardness can be measured for pre-grinding and post-grinding measurements on the running surface (the instrument converts from Leeb hardness values). However, it has to be noted that this study does not consider surface hardness measurements.

A calibrated modern hardness testing machine (type KB30) with a programmable work stage has been used for the experiments. Thus, the position of the hardness measurement points can be accurately selected.

The hardness measurements have been performed from the welding axis side of Slices #2, #3, #4, and #5, as shown in Fig. 6. The measurement points are 5 mm apart horizontally and 2 mm apart vertically. On average, 15 points were obtained per slice in the "x" direction (horizontally) and 11 points in the "y" direction (vertically).

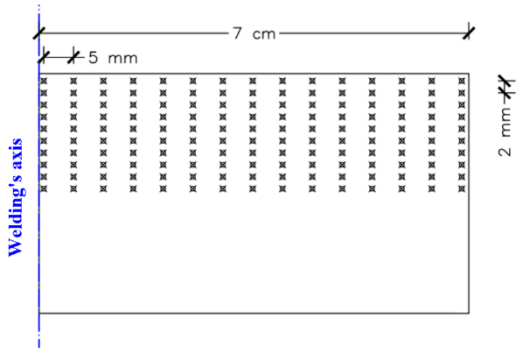

Fig. 6 Allocation of hardness measurement points

Expected results are the hardness profiles in the thermal response of the rail weld as a function of the longitudinal distance from the welding center axis for different configurations (consideration of different rail hardness, investigation of different welding technologies, joint and repair welds, etc.)

2.7 Microstructural analysis

Microstructural images of the nital etched specimens have been taken by Zeiss Axio Imager M1m optical microscope (Fig. 7) using brightfield illumination and objectives with magnifications of 5× and 20×.

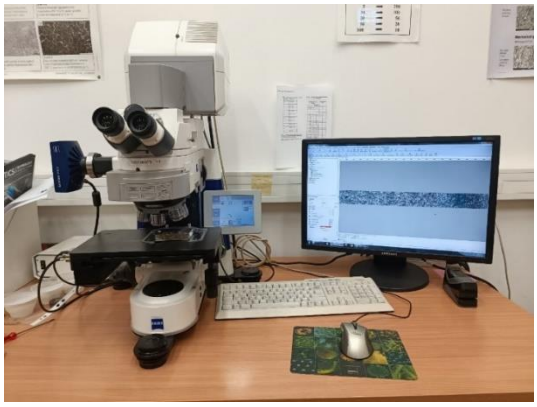

Fig. 7 Zeiss AxioImager M1m optical microscope

3. Results And Discussion

The hardness values have been plotted and examined in the function of the distance below the running surface (depth) and the distance from the welding axis.

Due to a large amount of data, different aspects were selected for analysis:

i. the hardness profile below the running surface (–0.5 mm) (comparing R260 data with SoW-5 [49] and Barna et al. [48], calculating surface hardness ratios) was investigated.
ii. the hardness profile at limit depth (20.5 mm below the running surface, i.e., –20.5 mm) (comparing R260 data with SoW-5 [49] and Barna et al. [48], calculating surface hardness ratios) was investigated. The limit depth means that the hardness values do not change in the rail below this value. It was determined based on the measurements.
iii. Depth hardness ratios were given for the R260 sides of the rails compared to the measurements published in [48].
iv. In selected perpendicular cross sections, the hardness profile has been determined and plotted in the horizontal direction (i.e., laterally).
v. 5× magnification macrostructure images have been used to visualize the parts of the HAZ.

vi. 20× magnification microstructure images have been joined with the corresponding hardness values.

It has to be mentioned that in the above point (i), the hardness measurements on the running surface have not been executed during the present study. Therefore, these data are related to the –0.5 mm depths. It is an approximation, however, it does not have too many errors.

In the present paper, a detailed analysis of the HAZ of TW of railway rails was carried out using laboratory tests on samples of welding performed in non-laboratory conditions.

The main objective of the tests was to see how the hardness of the rail steel in the heat-affected zone varies as a function of depth (i.e., distance from the running surface of the rail head) and distance from the welding centerline. A further objective was to link microstructural images to the hardness values.

Figs. 8-11 demonstrate the hardness variation of Slice #2s of Sample #1 (see Figs. 8 and 9), as well as Sample #2 (see Figs. 10 and 11) considering the –0.5 mm and –20.5 mm depth values under the rails' running surface (i.e., Figs. 8 and 10 show the –0.5 mm, and Figs. 9 and 11 demonstrate the –20.5 mm depths).

For type Sample #1, it can be concluded that the hardness increases from the welding axis to the heat-affected zone, reaches a maximum there, and then decreases drastically to a minimum at the outer edge. According to the trend described, the maximum value is approx. 40.5...45.5 mm from the weld axis, the minimum is approx. 10 mm further away. For Sample #2, the maximum hardness in the heat-affected zone is no longer an extreme value, the values are in a smaller range. The hardness gradually decreases to the minimum at the outer edge of the HAZ. Based on the described behavior, the hardness starts to decrease gradually after approx. 40.5...45.5 mm and reaches its minimum at a distance of approx. 50.5...55.5 mm from the welding axis.

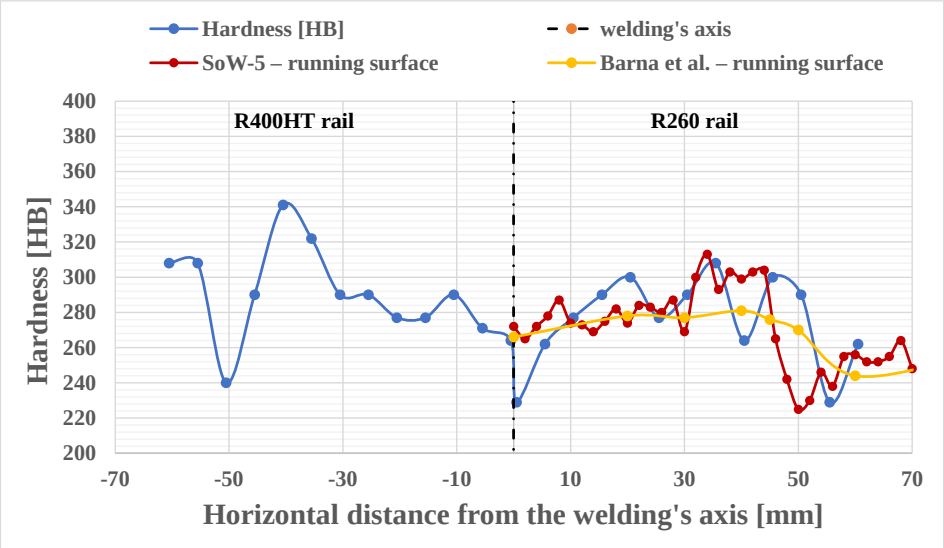

Fig. 8 Hardness variation at a depth of –0.5 mm below the running surface in Slice #2 of Sample #1 (considering the literature [48,49])

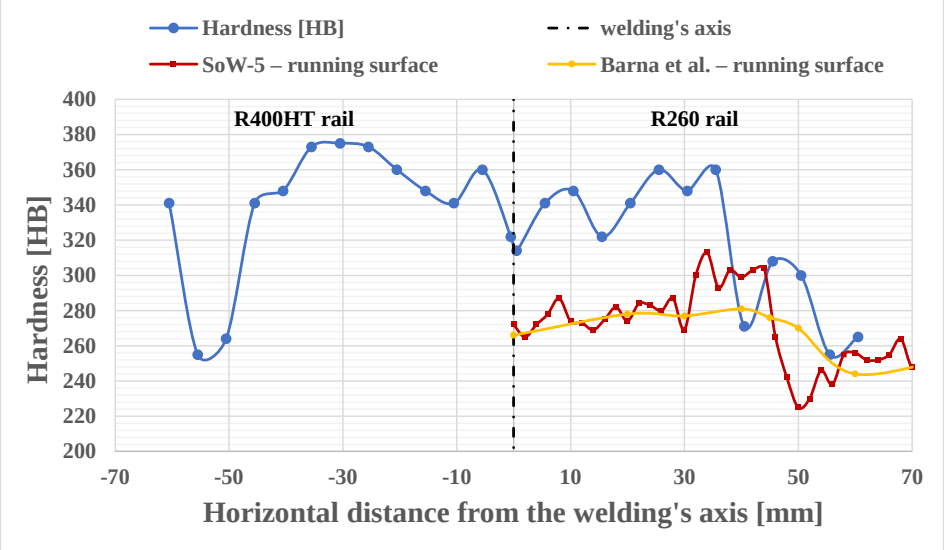

Fig. 9 Hardness variation at a depth of –0.5 mm below the running surface in Slice #2 of Sample #2 (considering the literature [48,49])

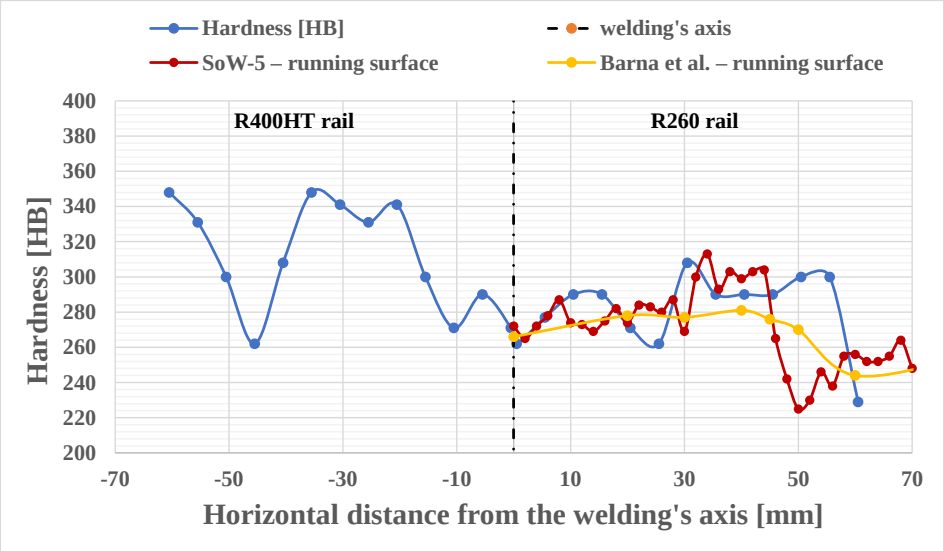

Fig. 10 Hardness variation at a limit depth (–20.5 mm below the running surface) in Slice #2 of Sample #1 (considering the literature [48,49])

At the limit depth (–20.5 mm) (see Figs. 10 and 11), the hardness values start to vary between smaller intervals. An extremely high value is no longer present in the thermal zone but in an upper "plateau". This "plateau" starts at approx. 20.5 mm from the welding axis,

and at approx. 40.5 mm, there is a gradual decrease to a minimum hardness. The hardening up to the base material value can be clearly seen in each diagram. This phenomenon is typical for all samples.

The above data were compared to the R260 rail's data with those of SoW-5 [49] and Barna et al. [48]. These graphs are depicted in Figs. 12-15. The shown data are calculated based on the averages of all Slices' results in the cases in question.

Analyzing the data related to 0.5 mm under the running surface, the highest surface area ratio is 50.5 mm from the welding's axis for Sample #1 (see Fig. 12), where the average of the measured data set reaches its maximum, and the SoW-5 data set reaches its minimum. The field surface area measurement is between the two values, so the field measurement deviates only 7% from 100%. Most of the data are lower than 100% hardness, so our averages are higher than the reference values but lower at 0.5, 40.5, and 60.5 mm from the welding axis.

When examining the surface hardness ratio, the majority of the data are lower than 100% hardness, so the calculated averages are higher than the reference values at a depth of –0.5 mm below the running surface at 40.5 mm from the weld axis. It was lower at a depth of –20.5 mm and extended to 60.5 mm for all samples.

In Figs. 16 and 17, the depth hardness ratio values are given. They are only calculated for the R260 sides of Sample #1 and Sample #2.

Based on Figs. 16 and 17, it can be concluded that the most critical zone of Sample #1 (see Fig. 16) is 40-60 mm from the welding's axis, in all depths. There are relatively high steps (jumps) in the hardness values at 50 mm from the welding's axis in a positive direction. It must be noted that the neighbor values are fluctuating at 100%. Compared to them, the measured values in Fig. 17 are very interesting. They are related to Sample #2. Between 0.5 and 20.5 mm from the welding's axis, the depth hardness ratio values are approximately 125-130%, there is a downstep to 95-105% (at 40.5 mm from the welding's axis), and from this point, an up step to 125-130% (it is at 50.5 mm from the welding's axis), and again a down step to 90-105%. The reason for this can be the different welding portions and the evolved variation.

At defined distances from the welding axis (10.5 mm, 25.5 mm, 35.5 mm, 50.5 mm, 70.5 mm), the horizontal hardness profile was investigated in cross sections perpendicular to the rail axis. This paper presents only the graphs related to +/–10.5 mm (see Figs. 18 and 19), however, the relevant results are discussed for all.

Up to a distance of approx. 35.5 mm from the welding axis, the hardness values of R260 and R400HT rails do not differ significantly, despite the hardness of the base material. The R400HT rail reaches higher hardness values from the edge of the HAZ. In the case of Sample #1, the R400HT rail approached the values of R260. In Sample #2, the R260 rail hardness approaches the hardness of the R400HT rail.

While the hardness profiles in the specimens of Sample #2 do not describe a characteristic behavior in either the welding zone or in the heat-affected zone, the hardness values of the rail R260 in Sample #1 increase from the rail axis.

The microstructure images at 5× magnification illustrate the HAZ sections (see Figs. 20 and 21). The procedure is similar to the published method and solution in [29]. The 20× magnification microstructure images were paired with the corresponding hardness values.

Six zones of the microstructure have been identified for Sample #1 (welding axis environment, welding edge, fused mixed zone, coarse-grained HAZ, fine-grained HAZ,

and intercritical HAZ). Sample #2 had five zones (welding axis environment, fused mixed zone, unvarying grain size HAZ, intercritical HAZ, and the base material).

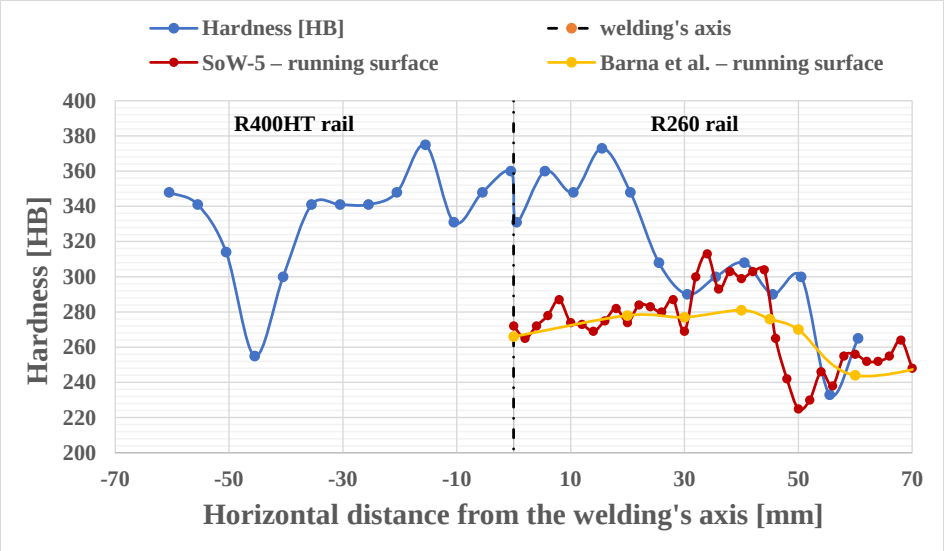

Fig. 11 Hardness variation at a limit depth (–20.5 mm below the running surface) in Slice #2 of Sample #2 (considering the literature [48,49])

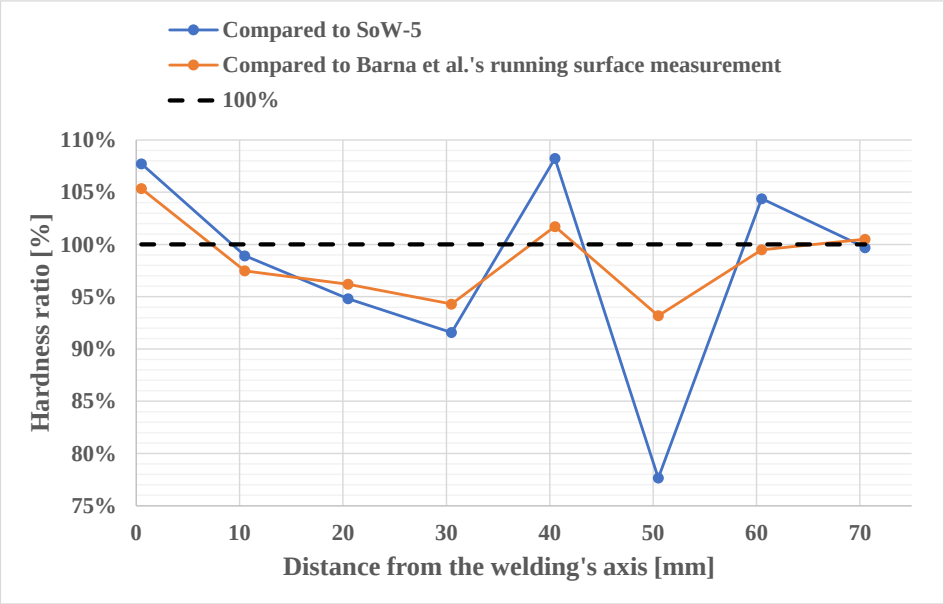

Fig. 12 Surface hardness ratio values of Sample #1 considering the –0.5 mm below the running surface (considering the literature [48,49])

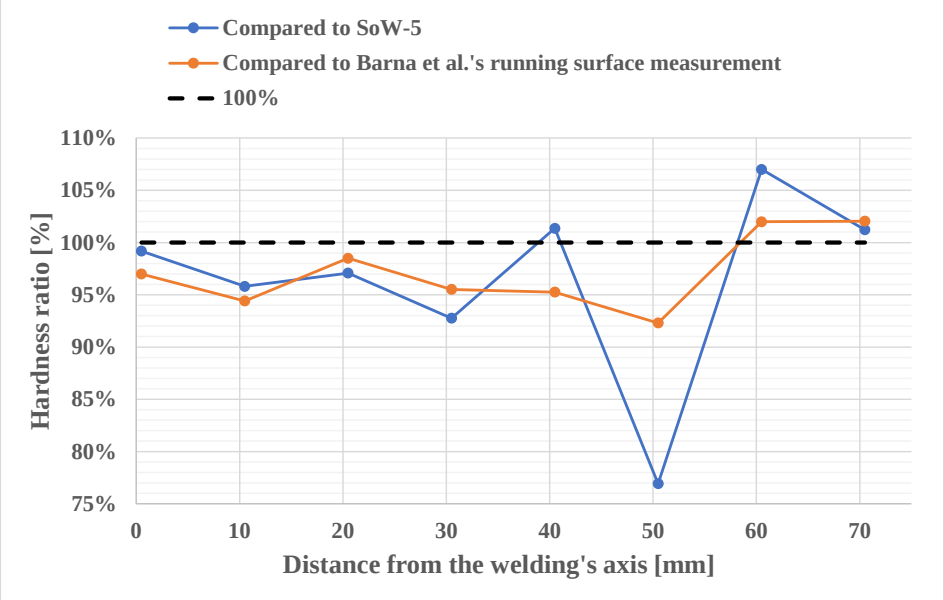

Fig. 13 Surface hardness ratio values of Sample #1 considering the –20.5 mm below the running surface (considering the literature [48,49])

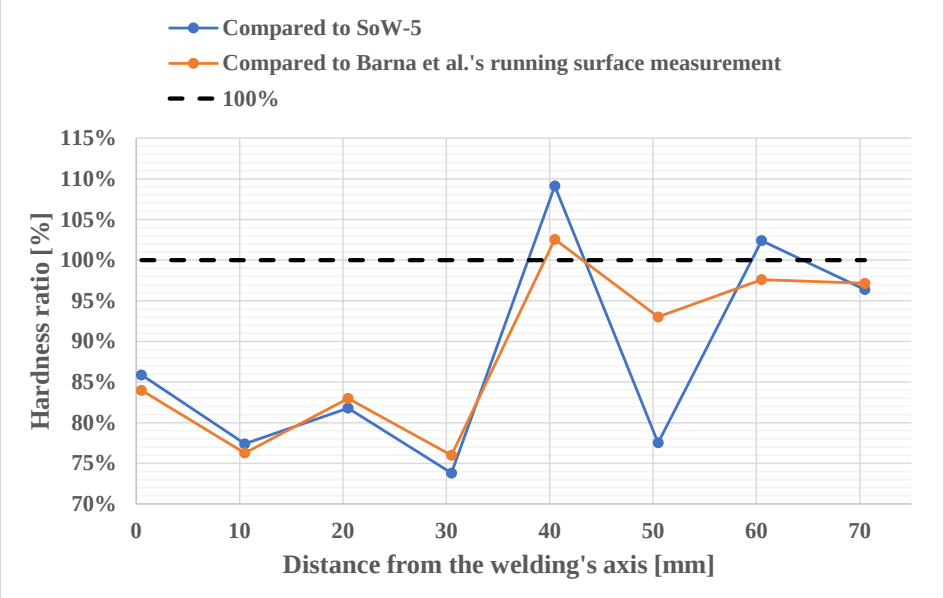

Fig. 14 Surface hardness ratio values of Sample #2 considering the –0.5 mm below the running surface (considering the literature [48,49])

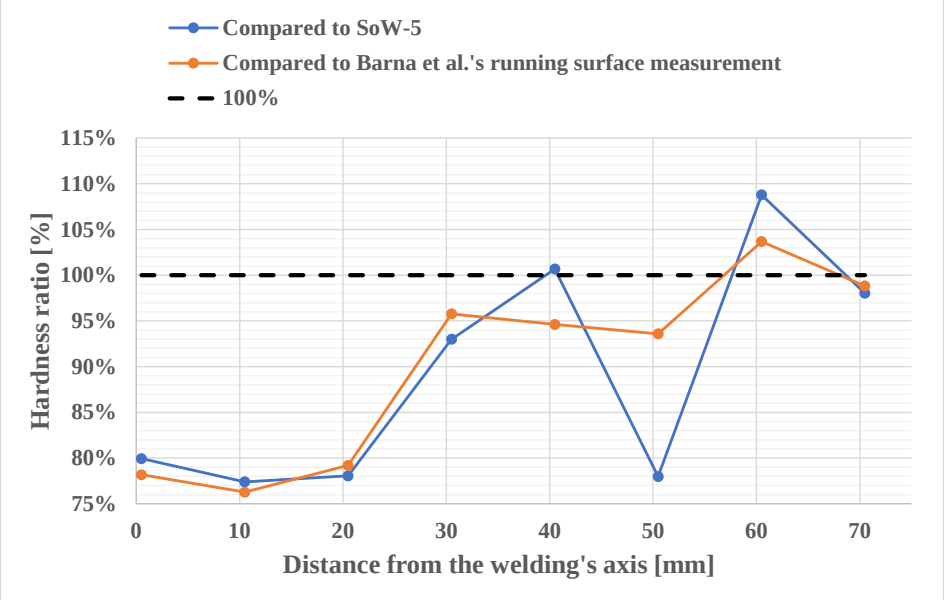

Fig. 15 Surface hardness ratio values of Sample #2 considering the –20.5 mm below the running surface (considering the literature [48,49])

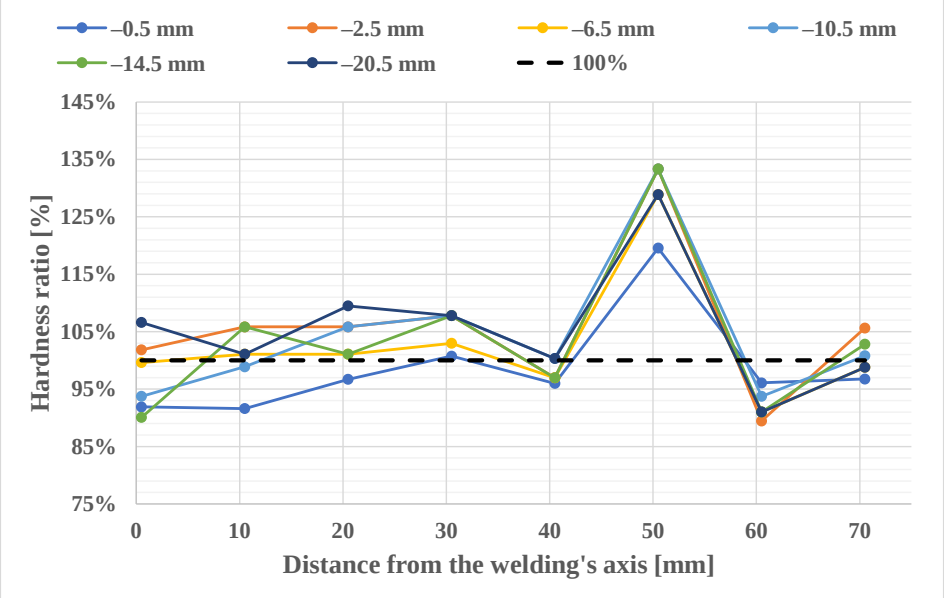

Fig. 16 Depth hardness ratio values of Sample #1 considering different depths. The comparisons were made according to the surface hardness values published in [48]

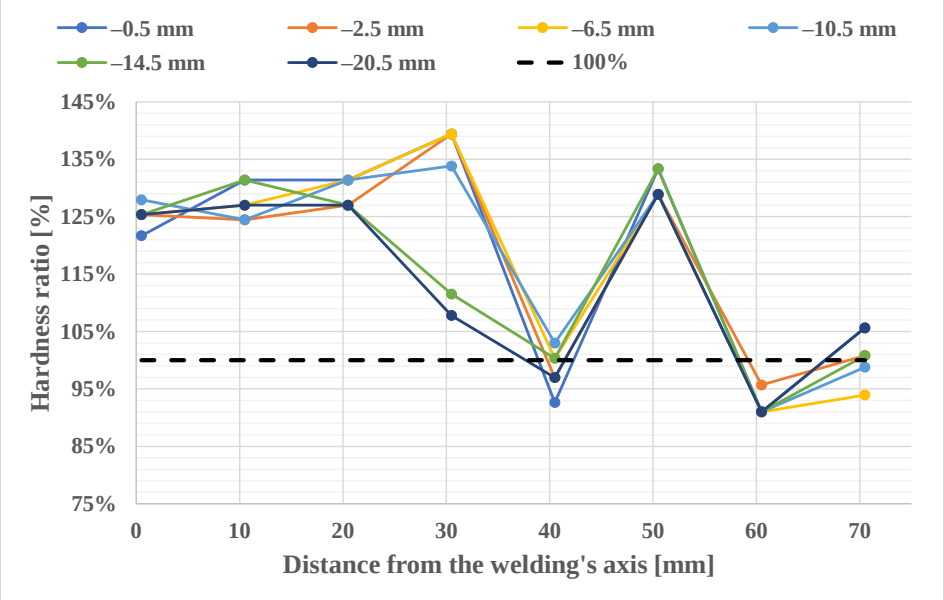

Fig. 17 Depth hardness ratio values of Sample #2 considering different depths. The comparisons were made according to the surface hardness values published in [48]

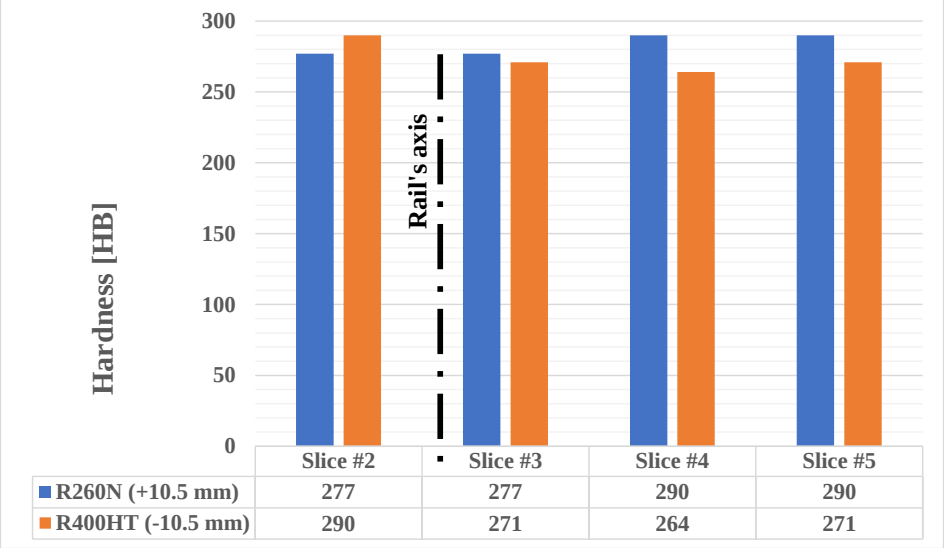

Fig. 18 Variation of hardness in +/–10.5 mm depth from the axis of welding for Sample #1 in the cross-section

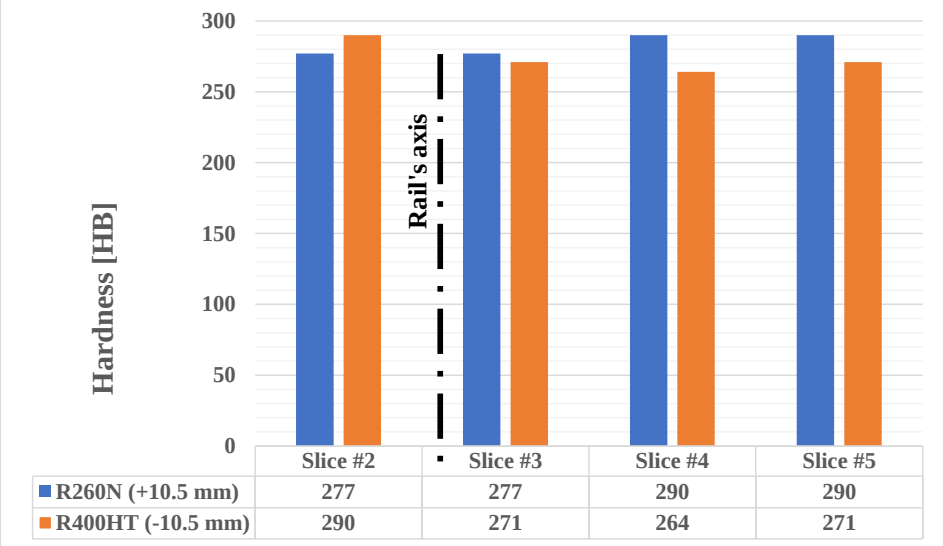

Fig. 19 Variation of hardness in +/–10.5 mm depth from the axis of welding for Sample #2 in the cross-section

After the decarbonization/centreline, grain growth was observed, followed by a fine-grained microstructure undergoing recrystallization. Partial austenitization between the fine-grained structure and the matrix characterizes the microstructure.

Fine pearlite grains and large coarse pearlite grains were formed as a function of the cooling rate. The faster the cooling velocity, the finer the grain size is.

Fine grains crystallize rapidly and form a hard and wear-resistant microstructure.

Coarse grains are characterized by slow crystallization with lower hardness values - a microstructure more sensitive to abrasion.

For the R260 rail, the weld zone is characterized by coarse grains and the heat-affected zone by fine grains.

For the R400HT rail, the hardness of the base material is the highest, in contrast to the previous case, where the grain size is the smallest.

The border of the recrystallization zone is located at approx. 50.5....60.5 mm from the welding axis. It causes an increase in ductility and a decrease in hardness. The phenomenon of softening can occur here.

Further conclusions can be derived from Figs. 8-21, but mainly Figs. 20 and 21:

- both weldings (i.e., Sample #1 and #2) generally have a hardness variation within 100 HB within a zone of 15-60 mm from the weldings' axis.
- Sample #1's lengthwise profile shows that within 10 mm of the HAZ (between 50-60 mm at the end of the HAZ) the hardness values drop 100 HB, which is extremely unfortunate. On the base material, it jumps immediately to 120 HB at 60-70 mm. It is a very critical 20 mm zone.
- There can be seen a similar phenomenon in the case of Sample #2's lengthwise profile: between 50 and 60 mm from the welding's axis, and there is a drop of

90 HB; then, within 60-70 mm, it jumps 90 HB. This 20 mm zone is more uniform.

- The weldings ensured and "brought" the results as expected, a more uniform hardness change can be obtained when applying the R350HT welding dose on the R400HT side (i.e., in the case of Sample #2).

Fig. 20 Hardness profile 0.5 mm below the running surface in case of weld Sample #1, Slice #3 – R400HT rail

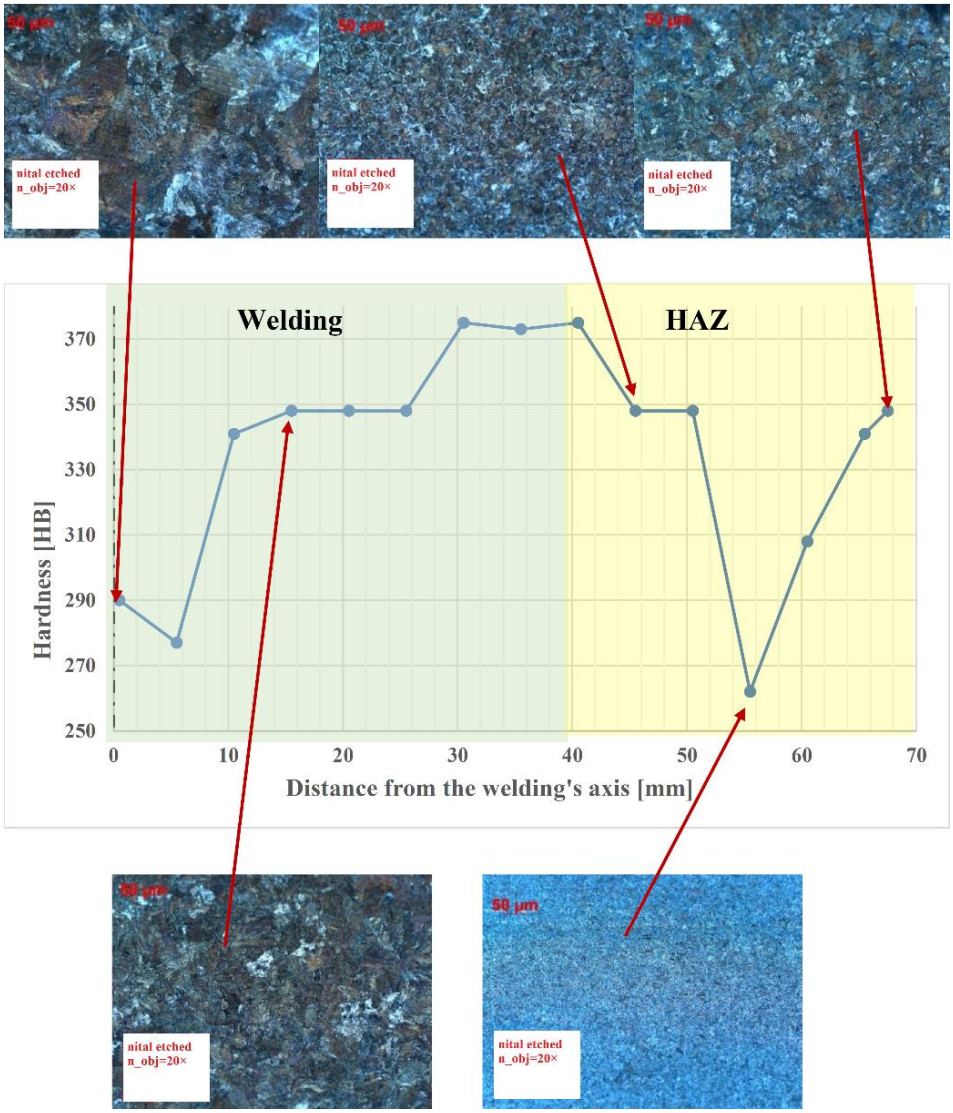

Fig. 21 Hardness profile 0.5 mm below the running surface in case of weld Sample #2, Slice #3 – R400HT rail

4. CONCLUSIONS

In this paper, special aluminothermic rail welding was investigated, where there was a two-step difference between the categories of welded rails. R260 and R400HT rails were welded together under non-laboratory but technologically strictly controlled precision conditions. The relevant technological instructions were entirely and precisely followed.

Two types of samples were prepared. For Sample #1, we used an R260 welding portion, and for Sample #2, a thermite portion for R350HT rails.

Based on the results of the laboratory hardness, macro-, and microstructural tests performed, it was found that Sample #2 gave more favorable results in running the hardness profiles. It means that if it is not possible to incorporate temporary intermediate hardness rails, it is preferable to weld in the two-step rail grade jump with the welding portion corresponding to the intermediate rail. Of course, to make a general statement, a considerable amount of further laboratory testing will be needed in the future, where it would be worthwhile to investigate several cases between R200 and R400HT (considering special, for example, bainitic rails, etc.), not only for Vignole rails but also for grooved rails and block rails.

Acknowledgement: *This paper was technically supported by the research team "SZE-RAIL". The authors thank Gerencsér, B. for English proofreading and editing.*

REFERENCES

1. Dobruszkes, F., 2011, *High-speed rail and air transport competition in Western Europe: A supply-oriented perspective*, Transport policy, 18(6), pp. 870-879.
2. Ramazan, B., Mussaliyeva, R., Bitileuova, Z., Naumov, V., Taran, I., 2021, *Choosing the logistics chain structure for deliveries of bulk loads: Case study of the Republic Kazakhstan*, Naukovyi Visnyk Natsionalnoho Hirnychoho Universytetu, 2021(3), pp. 142-147.
3. Nugymanova, G., Nurgaliyeva, M., Zhanbirov, Z., Naumov, V., Taran, I., 2021, *Choosing a servicing company's strategy while interacting with freight owners at the road transport market*, Naukovyi Visnyk Natsionalnoho Hirnychoho Universytetu, 2021(1), pp. 204-210.
4. Fischer, S., 2022, *Geogrid reinforcement of ballasted railway superstructure for stabilization of the railway track geometry – A case study*, Geotextiles and geomembranes, 50(5), pp. 1036-1051.
5. Šestaková, J., Ižvolt, L. Mečár, M., 2019, *Degradation-prediction models of the railway track quality*, Civil and Environmental Engineering, 15(2), pp. 115-124.
6. Dybeł, K., Kampczyk, A., 2022, *Sensitivity of Geometric Parameters in the Sustainability Development of Continuous Welded Rail*, Acta Technica Jaurinensis, 15(3), pp. 150-161.
7. Kampczyk, A., Dybeł, K., 2021, *Integrating surveying railway special grid pins with terrestrial laser scanning targets for monitoring rail transport infrastructure*, Measurement, 170, 108729.
8. Pultznerová, A., Mečár, M., Šestáková, J., Hodás, S., 2022, *Influence of the Condition of the Railway Superstructure on Traffic Noise on the Regional Line*, Civil and Environmental Engineering, 18(2), pp. 402-407.
9. Ahac, M., Ahac, S., Lakušić, S., 2022, *Evaluation of non-acoustic properties of traffic noise walls*, Građevinar, 74(1), pp. 35-49.
10. Csortos, G., Augusztinovicz, F., Bocz, P., 2021, *Optimal operation of a rail lubrication device with respect to noise reduction and wheel/rail friction coefficient*, Acta Technica Jaurinensis, 14(2), pp. 138-154.
11. Šestáková, J., Matejov, A., Pultznerová, A., 2022, *Rehabilitation of railway track quality in relation to diagnostic data*, XXX Russian-Polish-Slovak Seminar Theoretical Foundation of Civil Engineering (RSP 2021), Moscow, pp. 197-206.
12. Kuchak, A.J.T., Marinkovic, D., Zehn, M., 2021, *Parametric Investigation of a Rail Damper Design Based on a Lab-Scaled Model*, Journal of Vibration Engineering and Technologies, 9(1), pp. 51-60.
13. Kuchak, A.J.T., Marinkovic, D., Zehn, M., 2020, *Finite element model updating - Case study of a rail damper*, Structural Engineering and Mechanics, 73(1), pp. 27-35.
14. Macura, D., Laketić, M., Pamučar, D., Marinković, D., 2022, *Risk Analysis Model with Interval Type-2 Fuzzy FMEA – Case Study of Railway Infrastructure Projects in the Republic of Serbia*, Acta Polytechnica Hungarica, 19(3), pp. 103-118.
15. Heyder, R., Girsch, G., 2005, *Testing of HSH(R) rails in high-speed tracks to minimise rail damage*, Wear, 258(7-8), pp. 1014-1021.
16. Németh, A., Fischer, S., 2021, *Investigation of the glued insulated rail joints applied to CWR tracks*, Facta Universitatis,-Series Mechanical Engineering, 19(4), pp. 681-704.

17. Ilić, N., Jovanović, M.T., Todorović, M., Trtanj, M., Šaponjić, P., 1999, *Microstructural and mechanical characterization of postweld heat-treated thermite weld in rails*, Materials characterization, 43(4), pp. 243-250.
18. Josefson, B.L., Ringsberg, J.W., 2009, *Assessment of uncertainties in life prediction of fatigue crack initiation and propagation in welded rails*, International journal of fatigue, 31(8-9), pp. 1413-1421.
19. Skyttebol, A., Josefson, B.L., Ringsberg, J.W., 2005, *Fatigue crack growth in a welded rail under the influence of residual stresses*, Engineering Fracture Mechanics, 72(2), pp. 271-285.
20. Jezzini-Aouad, M., Flahaut, P., Hariri, S., Zakrzewski, D., Winiar, L., 2010, *Improving fatigue performance of alumino-thermic rail welds*, Applied Mechanics and Materials, 24-25, pp. 305-310.
21. Schroeder, L.C., Poirier, D.R., 1984, *The mechanical properties of thermite welds in premium alloy rails*, Materials science and engineering, 63(1), pp. 1-21.
22. Schroeder, L.C., Poirier, D.R., 1985, *Structure and properties of thermite welds in premium rails*, U.S. Department of Transportation, Federal Railroad Administration, Office of Research and Development, Washington DC, Final report, No. DOT/FRA/ORD-85/02, pp. 1-110.
23. Meriç, C., Atık, E., Şahın, S., 2002, *Mechanical and metallurgical properties of welding zone in rail welded via thermite process*, Science and technology of welding and joining, 7(3), pp. 172-176.
24. Galay, M.S., Ilinykh, A.S., 2021, *Improving the technology of aluminothermic rail welding based on software simulation*, Journal of Physics: Conference Series, 1967(1), 012063.
25. Porcaro, R.R., Faria, G.L., Godefroid, L.B., Apolonio, G.R., Cândido, L.C., Pinto, E.S., 2019, *Microstructure and mechanical properties of a flash butt welded pearlitic rail*, Journal of materials processing technology, 270, pp. 20-27.
26. Sarikavak, Y., Turkbas, O.S., Cogun, C., 2020, *Influence of welding on microstructure and strength of rail steel*, Construction and Building Materials, 243, 118220.
27. Tancsics, F., Ibriksz, T., 2020, *Determining the optimum heating time of small sized test specimen made from weldable mild steel*, IOP Conference Series: Materials Science and Engineering, 903(1), 012033.
28. European Committee for Standardization, 2020, *EN ISO 643:2020, Micrographic determination of the apparent grain size*, 28 p.
29. Liu, Y., Tsakadze, Z., Hoh, H.J., Pang, J.H.L., Christian, I., Ng, T.X., Ng, Y.F., 2018, *Mechanical properties and microstructural analysis of rail thermite welding joints*, 2018 International Conference on Intelligent Rail Transportation (ICIRT), Singapore, 2018, doi: https://doi.org/10.1109/ICIRT.2018.8641675.
30. Mutton, P.J., Alvarez, E.F., 2004, *Failure modes in aluminothermic rail welds under high axle load conditions*, Engineering Failure Analysis, 11(2), pp. 151-166.
31. Kurhan, D.M., Fischer, S., 2022, *Modeling of the dynamic rail deflection using elastic wave propagation*, Journal of Applied and Computational Mechanics, 8(1), pp. 379-387.
32. Sysyn, M.P., Nabochenko, O.S., Kovalchuk, V.V., Przybylowicz, M., Fischer, S., 2021, *Investigation of interlocking effect of crushed stone ballast during dynamic loading*, Reports in Mechanical Engineering, 2(1), pp. 65-76.
33. Jóvér, V., Gáspár, L., Fischer, S., 2022, *Investigation of Tramway Line No. 1, in Budapest, Based on Dynamic Measurements*, Acta Polytechnica Hungarica, 19(3), pp. 65-76.
34. Jóvér, V., Fischer, S., 2022, *Statistical analysis of track geometry parameters on tramway line No. 1 in Budapest*, Baltic Journal of Road and Bridge Engineering, 17(2), pp. 75-106.
35. Jóvér, V., Sysyn, M., Liu, J., Fischer, S., 2023, *Geometry variation of ballasted railway tracksdue to weather conditions*, Naukovyi Visnyk Natsionalnoho Hirnychoho Universytetu, 2023(1), pp. 74-79.
36. Szalai, S., Kocsis Szürke, S., Harangozó, D., Fischer, S., 2022, *Investigation of deformations of a lithium polymer cell using the Digital Image Correlation Method (DICM)*, Reports in Mechanical Engineering, 3(1), pp. 116-134.
37. Harangozó, D., Kozma, I., Czinege, I., Szalai, S., 2022, *Analysis of inhomogeneous deformation occurring during post-necking phase of tensile test*, IOP Conference Series: Materials Science and Engineering, 1246(1), 012018.
38. Szalai, S., Harangozó, D., Czinege, I., 2019, *Characterisation of diffuse and local necking of Aluminium alloy sheets using DIC technique*, Acta Technica Jaurinensis, 12(3), pp. 191-204.
39. Szalai, S., Szívós, B.F., Kurhan, D., Németh, A., Sysyn, M., Fischer, S., 2023, *Optimization of Surface Preparation and Painting Processes for Railway and Automotive Steel Sheets*, Infrastructures, 8(2), 28.
40. Szalai, S., Fehér, V., Kurhan, D., Németh, A., Sysyn, M., Fischer, S., 2023, *Optimization of Surface Cleaning and Painting Methods for DIC Measurements on Automotive and Railway Aluminum Materials*, Infrastructures, 8(2), 27.
41. Szalai, S., Eller, B., Juhász, E., Movahedi Rad, M., Németh, A., Harrach, D., Baranyai, G., Fischer, S., 2022, *Investigation of deformations of ballasted railway track during collapse using the Digital Image Correlation Method (DICM)*, Reports in Mechanical Engineering, 3(1), pp. 168-191.
42. Messaadi, M., Grossoni, I., Shackleton, P., Shevtsov, I., Bezin, Y., Dollevoet, R., 2021, *Rail degradation due to thermite weld discontinuities: Field experience*, Engineering Failure Analysis, 128, 105585.

43. Josefson, B.L., Bisschop, R., Messaadi, M., Hantusch, J., 2020, *Residual stresses in thermite welded rails: significance of additional forging*, Welding in the World, 64, pp. 1195-1212.
44. Salehi, I., Kapoor, A., Mutton, P., 2011, *Multi-axial fatigue analysis of aluminothermic rail welds under high axle load conditions*, International Journal of Fatigue, 33(9), pp. 1324-1336.
45. Chen, Y., Lawrence, F.V., Barkan, C.P., Dantzig, J.A., 2006, *Heat transfer modelling of rail thermite welding*, Proceedings of the Institution of Mechanical Engineers, Part F: Journal of Rail and Rapid Transit, 220(3), pp. 207-217.
46. European Committee for Standardization, 2011, *EN 13674-1:2011, Railway applications. Track. Rail. Part 1: Vignole railway rails 46 kg/m and above*, 123 p.
47. Hungarian State Railways, 2010, *Welding of railway rails*, Hungarian State Railways, Budapest, 102 p. (in Hungarian)
48. Barna, V., Brautigam, A., Kocsis, B., Harangozó, D., Fischer, S., 2022, *Investigation of the Effects of Thermit Welding on the Mechanical Properties of the Rails*, Acta Polytechnica Hungarica, 19(3), pp. 37-49.
49. https://www.gt-railservice.com/fileadmin/user_upload/PDF/Schienenverbindung/SOW-5_DE-EN-FR.pdf (last access: 17.12.2022)
50. European Committee for Standardization, 2018, *MSZ EN ISO 6507-1:2018, Metallic materials. Vickers hardness test. Part 1: Test method*, 39 p.